Pergamon

Journal of Structural Geology, Vol. 18, Nos 2/3, pp. 235 to 248, 1996

0191-8141/96 $15.00 + 0.00

0191-8141(96)00115-8

The shapes, major axis orientations and displacement patterns of fault surfaces

A. NICOL, J. WATTERSON, J. J. WALSH and C. CHILDS

Fault Analysis Group, Department of Earth Sciences, University of Liverpool, Liverpool L69 3BX, U.K.

(*Received* 9 *January* 1995; *accepted in revised form* 23 *August* 1995)

Abstract—Displacement contour diagrams constructed using seismic reflection data and coal-mine plans are analysed to establish the factors determining the dimensions, shapes and displacement patterns of normal faults. For blind isolated normal faults in layered sequences the average aspect ratio is 2.15, with sub-horizontal major axes. Earthquake slip-surface aspect ratios range from 0.5 to 3.5 and are independent of slip orientation. The principal control on the shape of blind isolated faults is mechanical anisotropy associated with rock layering, resulting in layer-parallel elongation of fault surface ellipses. Faults that intersect the free surface and/or interact with nearby faults have aspect ratios ranging from 0.5 to 8.4, and are referred to as restricted. Restriction of fault growth has various effects including: (i) reduced curvature of the tip-line and of displacement contours; and (ii) increased displacement gradients in the restricted region. Many faults are restricted at more than one place on their tip-line loop and so have highly irregular shapes and displacement patterns. Subsequent linkage of interacting faults produces combined faults with aspect ratios within the normal range for unrestricted faults. Lateral interaction between faults does not necessarily lead to a change in the power-law exponent of the fault population.

INTRODUCTION

Simple normal faults have been shown to have an approximately elliptical shape with the major axis sub-horizontal (Rippon 1985a,b, Barnett *et al.* 1987, Walsh & Watterson 1989). An elliptical tip-line, with elliptical displacement contours concentric about a centrally located maximum displacement, has been found to be a useful idealization although few real faults conform to this ideal. A fault surface approximating this pattern (Fig. 1) illustrates the terminology used for the principal dimensions of fault surfaces. The atypical near-equidimensional form of this fault surface is referred to in a later section. The aspect ratios quoted throughout this paper are calculated as the fault strike dimension/dip dimension; values >1.0 indicate horizontal elongation.

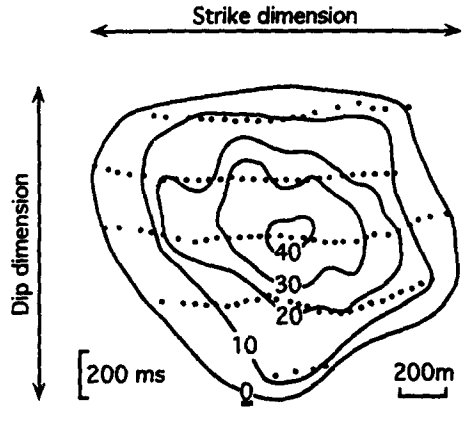

Fig. 1. Displacement contour diagram for a normal fault from a Gulf Coast three-dimensional seismic data set. The view is normal to the fault surface and throw contours are expressed as two-way travel-time (ms, 1 ms ~ 1.25 m) and are constructed from 106 throw readings (dots) on five horizons. Throw resolution is 5–10 ms and the position of the true fault tip-line is estimated by extrapolation of throw gradients to zero throw. Tip-line positions estimated in this way are indicated on all diagrams by 0. Maximum throw is 42 ms (*ca* 53 m), strike dimension is *ca* 1.5 km and aspect ratio *ca* 1.0. Vertical and horizontal scales are approximately equal.

An obvious question is why surfaces of simple faults are elliptical and what determines the alignment of their major axes? It has previously been suggested (Rippon 1985a, Walsh & Watterson 1989) that the ellipticity could be due either to the mechanical heterogeneity of the rock sequence, or to the energy differences between screw and edge dislocations which would result in elliptical fault surfaces even in mechanically isotropic rock; there were then insufficient data to guide a choice between these alternatives.

A severe limitation of all previously published data relating to the form of fault surfaces is that they have concerned only dip-slip faults. This limitation has now been circumvented by establishing, from the loci of their aftershocks, the shapes and alignments of normal dip-slip, reverse dip-slip, oblique-slip and strike-slip earthquake generating main-shock slip-surfaces (see Table 2). Although we assume that these neotectonic slip-surfaces are equivalent to single fault surfaces, i.e. that the main-shocks are characteristic earthquakes in the sense of Schwartz & Coppersmith (1984), the conclusions are independent of this assumption.

A second question concerns the more frequent occurrences of fault surfaces which are not elliptical but of a form which is some distinctive and systematic derivative of an ellipse.

Individual faults generally represent one element of a fault system in which many faults kinematically interact

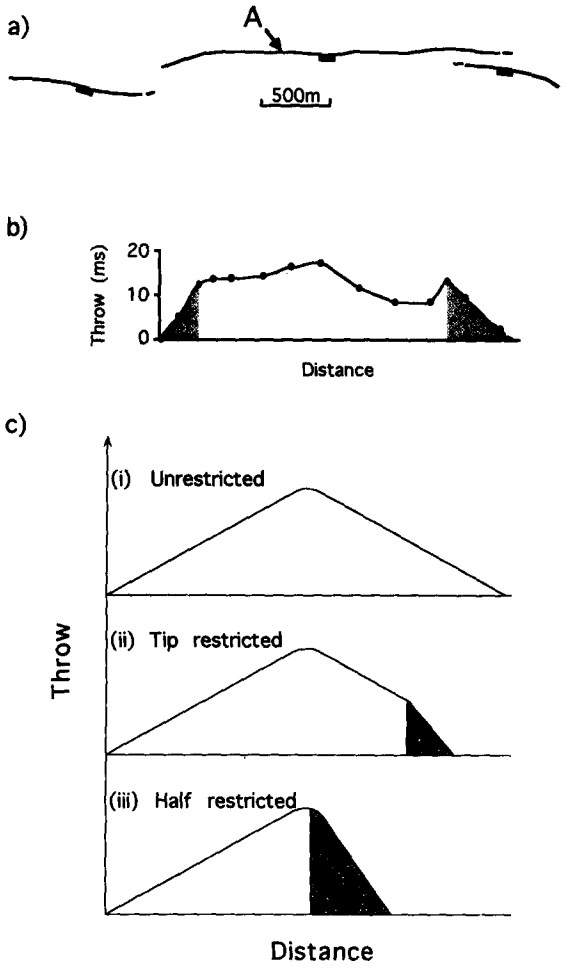

Fig. 2. (a) Fault map showing a normal fault trace, labelled A, restricted at both lateral tip-points by adjacent faults. (b) Horizontal throw profile for the restricted fault in (a), the restricted parts of the fault trace (stippled) have throw gradients significantly higher than elsewhere. The horizontal scales in (a) and (b) are the same. (c) Schematic diagram illustrating the three main types of fault displacement profile for: (i) unrestricted faults; (ii) faults restricted only towards a tip-point; and (iii) faults which are 50% restricted, i.e. between the point of maximum throw and the tip-point. Restricted parts of the throw profiles are stippled. Each profile type may occur along any orientation on a fault surface.

with one another. The likelihood of fault interaction increases with increase in fault system maturity with consequent increase in both the sizes and density of the component faults (Fig. 2). Because of such interactions we distinguish between *restricted* and *unrestricted* fault surfaces (Fig. 2c). Unrestricted faults are blind and effectively isolated faults whose growth has not been perturbed by intersection with, or close approach to either the free surface or to substantial layers or bodies of incompetent rock, e.g. salt, or to other faults. Surfaces of unrestricted faults have regular forms and approximate to simple ellipses with two lines of bilateral symmetry. Surfaces of the vast majority of faults are less regular with either one line of bilateral symmetry or none. The growth of these less regular faults has been perturbed by interaction with other structures, and they are referred to as restricted. Such faults are identified by increased displacement gradients close to the confining feature (e.g. adjacent fault, free surface or thick incompetent shale or salt layer). Gradients are either markedly higher close to a part of the fault tip-line than elsewhere (Fig. 2c ii), or higher on one half of a fault than on the other (Fig. 2c iii). Figures 2 (a) & (b) show an example in which throws decrease rapidly towards the lateral tips of a fault which relays displacement to adjacent faults; the fault is therefore restricted. As in Fig. 2 we do not attempt to distinguish between individual fault surfaces which originated independent of other nearby faults and those which are segments of a larger segmented fault (see Anders & Schlische 1994, Cartwright *et al.* 1995, Dawers & Anders 1995). Fault surfaces which are continuous on one scale of observation may, of course, be segmented when observed at a smaller scale, or visa versa. Both vertical and horizontal throw gradients have been used to identify growth restriction, although the latter generally are based on higher data densities and are correspondingly more reliable. Our analyses are restricted to relatively simple examples of restricted and unrestricted faults.

SHAPE, ALIGNMENT AND THROW DISTRIBUTIONS OF UNRESTRICTED FAULT SURFACES

Fault data

Throw contour diagrams, as in Fig. 1, have been examined for 35 wholly or partially unrestricted normal faults and their principal dimensions plotted (Fig. 3). Approximately 500 faults were examined and unrestricted fault data were extracted where at least one quadrant of a fault surface conformed with the criteria described above. Only three faults in the data set are classified as wholly unrestricted. Where necessary, measurements of a single quadrant have been doubled to provide values for a nominal entire fault with the same

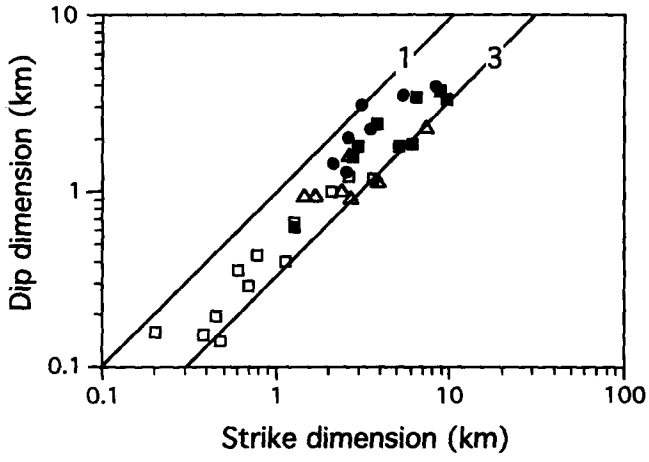

Fig. 3. Dip dimension vs strike dimension for nominally unrestricted faults from four regions (see Table 1): Derbyshire coal-field (open squares, $n = 12$), Timor Sea (filled squares, $n = 9$), Gulf Coast (filled circles, $n = 7$) and North Sea (open triangles, $n = 7$). In each case the fault dimensions were derived from at least one quadrant of the fault surface. Three faults are wholly unrestricted, two coal-field faults and one Gulf Coast fault (see text for further discussion). Straight lines correspond to aspect ratios of 1 and 3.

Table 1. Details of the four data sets for unrestricted faults plotted in Fig. 3. Data from the Derbyshire coal-field are from coal-seam plans, the remainder are from two- and three-dimensional offshore reflection seismic data sets

Name and location	Lithologies	Vertical interval sampled (km)	Number of faults	Aspect ratio (av.)
Derbyshire Coal mines, U.K.	Carboniferous sandstone, shale and coal	0.6	12	2.3
Timor Sea	Cenozoic limestone, claystone and sandstone	1.6	9	2.2
Gulf Coast	Late Miocene to recent sandstone with minor shales	3.7	7	1.6
North Sea	Jurassic sandstone and shales	1.8	7	2.4

characteristics as that quadrant. For faults which are wholly unrestricted nominal dimensions (derived by doubling quadrant dimensions) and actual dimensions differ by on average *ca* 10%. The throw contour diagrams are constructed from faults recorded on multiple horizons (3–20) in the coal-mine plan or reflection seismic data sets (Table 1). The tip-lines derived initially do not represent zero throw contours but are limited by the throw resolutions of the data sets. The resolution of the coal-mine data (*ca* 60 cm) is better than those of the seismic data, which are between 10 and 30 m. To minimize resolution effects on fault dimension data we have estimated real tip-lines, i.e. zero throw contours, by extrapolation using throw gradients close to the observed tip-lines; dimensions given are nevertheless regarded as minimum values. The shapes of the actual tip-lines are not expected to differ significantly from those of the observed tip-line loops.

Four geographical regions of different lithological character are represented in approximately equal proportions (see Table 1) and fault sizes for the entire data set range over 1.5–2.0 orders of magnitude according to the size attribute considered. Maximum fault throws range from 0.4 to 460 m, strike dimensions from 0.2 to 12 km and dip dimension from 0.15 to 5 km. Aspect ratios of fault surfaces, actual or nominal, range from 1.0 to 3.4 and the mean of 2.15 is close to that reported by Walsh & Watterson (1989). Mean aspect ratios for the individual regions from which the fault sample is derived are shown in Table 1 and indicate a distinctly lower mean for Gulf Coast faults. In all cases the major axes are sub-horizontal.

Average throw gradients along both major and minor principal semi-axes have been calculated for each fault. The gradients for the major and minor axes are referred to as horizontal and vertical throw gradients, respectively. Because the strike dimensions of unrestricted faults are about twice the dip dimensions, vertical displacement gradients are approximately double the horizontal gradients. Throw gradients are generally lower on smaller faults. Gradients on coal-field faults, with strike dimensions of 0.2–2.6 km, range from 0.001 to 0.007 (horizontal) and from 0.007 to 0.03 (vertical) and are lower than those on seismically imaged faults which have strike dimensions of 1.3–9.7 km and gradients of 0.007–0.06 (horizontal) and 0.04–0.22 (vertical). The increase in throw gradients with size is implicit in the fault displacement–dimension relationships of Walsh & Watterson (1989), Marrett & Allmendinger (1991) and Gillespie *et al.* (1992) which have power-law exponents >1.0, i.e. during growth displacement increases proportionally more than dimension.

Earthquake slip-surface data

The shapes and major axis orientations of main-shock slip-surfaces, as defined by aftershock loci, have been compiled for 54 earthquakes of mainly moderate magnitude (Table 2). Dimensions derived in this way are likely to be slightly larger than those of the actual slip-surfaces (Mendoza & Hartzell 1988), and the estimates also have uncertainties associated with aftershock locations. These uncertainties do not significantly affect the measured shapes of the slip-surfaces. Main-shock slip-surfaces were excluded from our analysis if the aftershocks were either poorly located or too few. Standard errors of aftershock locations for the earthquakes in Table 2 are generally <2 km vertically and ≤1 km laterally. Slip-surface dimensions calculated for this study have been compared with those of Wells & Coppersmith (1994) for the same events. Our aspect ratios differ by on average 0.29 (range 0–1.1) from those given by Wells & Coppersmith (1994), but for the purposes of this study the differences are not critical. Main-shock slip-surface dimensions given in Table 2 are averages of our measurements and those of Wells & Coppersmith (1994). Focal mechanism data are used to estimate the ratio of strike-slip to dip-slip movement for each of the slip-surfaces. Slip is categorized as oblique-slip when the strike-slip/dip-slip ratio is between 0.5 and 2.0. Slip-surfaces with a well defined sub-horizontal lower tip-line at an appropriate depth are assumed to intersect the base of the seismogenic layer and have been excluded. About 25% of the earthquake slip-surfaces in Table 2 intersect the free surface and have also been excluded from consideration.

Slip-surface dimension data are plotted in Fig. 4 with normal and reverse dip-slip, oblique-slip and strike-slip events distinguished. Aspect ratios range from 0.5 to 3.5 with a mean of *ca* 1.4 which is closer to the mean for Gulf Coast faults than to the mean for the entire fault data set. Mean aspect ratios for each slip-surface type vary by only ±0.1 from that for the entire slip-surface data set and within each type the typical major axis is sub-horizontal. Unlike the unrestricted fault data set, slip-surfaces which have interacted with nearby faults often

Table 2. Locations, parameters and published sources of the data plotted in Figs. 4–6. The 54 main-shock slip-surfaces (earthquake magnitudes M = 4.2–6.8) are defined by the distribution of earthquake aftershocks. Both aftershock and focal mechanism data are used to estimate fault dips. Slip-surfaces intersecting the free surface are indicated by (*) in the aspect ratio column

	Date	Earthquake	Magnitude (M_s)	Strike dimension (km)	Dip dimension (km)	Aspect ratio	Dip (°)	Depth to fault centre (km)	References
		Normal-slip							
1	06.06.77	Lorca, Spain	4.2 (M_b)	6	4	1.5	60	6	Mezuca *et al.* 1984
2	28.03.75	Pocatello Valley, Idaho, U.S.A	6.0	13.8	8.5	1.6	50	6.5	Arabasz *et al.* 1981
3	29.02.80	Arundy, France	4.9 (M_b)	4.9	5.5	0.9	78	3.8	Gagnepain-Beyneix *et al.* 1982
4	13.12.82	Dhamer, North Yemen	6.0	19.5	8.5	2.3*	32	4	Langer *et al.* 1987a
5	29.04.84	Perugia, Italy	5.2	17	6.5	2.6	55	5	Haessler *et al.* 1988
6	07.05.84	Lazio-Abruzzo, Italy	5.8	6.5	9	0.7	50	11	Westaway *et al.* 1989
7	13.09.86	Kalamata, Greece	5.8	16	12	1.3*	60	6	Lyon-Caen *et al.* 1988
		Strike-slip							
8	26.03.63	Wakasa Bay, Japan	6.5	20	8	2.5	68	6	Abe 1974
9	28.06.66	Parkfield, California, U.S.A.	6.0	35	10	3.5*	80	6	Eaton *et al.* 1970
10	12.09.66	Truckee, California, U.S.A.	5.8	11.5	8	1.4	80	5	Tsai & Aki 1970
11	09.09.69	Gifu, Japan	6.3	18	10	1.8	—	—	Purcaru & Berckhemer 1982
12	17.08.76	Kawazu, Japan	5.4	9	4	2.3	—	—	Purcaru & Berckhemer 1982
13	22.11.77	Willits, California, U.S.A.	4.8 (M_l)	4.5	7.5	0.6	76	9	Warren *et al.* 1985
14	09.03.78	Swabian Jura, Germany	5.3	7.5	8	0.9	84	5	Haessler *et al.* 1980
15	04.10.78	Wheeler Crest, California, U.S.A.	5.1	6.5	7	0.9	70	15	Peppin *et al.* 1989
16	06.08.79	Coyote Lake, California, U.S.A.	5.7	15	9.5	1.6*	76	7.5	Reasenberg & Ellsworth 1982
17	29.06.80	Izu-Hanto-Toho-Oki, Japan	6.2	14	9	1.6	73	9	Ishida 1984
18	27.07.80	Sharpsburg, Kentucky, U.S.A.	4.7	5	5.5	0.9	58	12	Herrmann *et al.* 1982
19	14.02.81	Elk Lake, Washington, U.S.A.	4.8	6	7	0.9	75	8	Grant *et al.* 1984
20	24.04.84	Morgan Hill, California, U.S.A.	6.1	28	8.5	3.3	82	6.5	Bakun *et al.* 1984
21	14.08.84	Sutton, Talkeetn. Alaska, U.S.A.	5.2	8.5	7	1.2	76	17	Lahr *et al.* 1986
22	14.09.84	Naganoken-Seibu, Japan	6.1	13	9.5	1.4	65	6.5	Takeo & Mikami 1987
23	23.11.84	Round Valley, California, U.S.A.	5.7	7	7.5	0.9	80	10	Smith & Priestley 1993
24	27.10.85	Constantine, Algeria	5.9	23	12	1.9*	84	6	Bounif *et al.* 1987
25	08.07.86	North Palm Springs, California, U.S.A.	6.0	17.5	10	1.8	46	14	Jones *et al.* 1986
26	21.07.86	Chalfant Valley, California, U.S.A.	6.2	20	11.5	1.7	55	9	Pacheco & Nábělek 1988
27	10.10.86	San Salvador, El Salvador	5.4	7	8.3	0.8	78	7	Harlow *et al.* 1993
28	10.06.87	Wabash Valley, Illinois, U.S.A.	4.4	2	3	0.7	80	11	Langer & Bollinger 1991
29	24.11.87	Elmore Ranch, California, U.S.A.	6.2	28.5	11	2.6*	73	6	Magistrale *et al.* 1989
30	24.11.87	Superstition Hills, California, U.S.A.	6.6	30	11	2.7*	79	6	Magistrale *et al.* 1989
31	03.12.88	Pasadena, California, U.S.A.	4.2	4.3	3	1.4	66	14.5	Heaton 1989
32	02.28.90	Upland, California, U.S.A.	5.5	4	8	0.5	72	8	Allen *et al.* 1990
33	23.04.92	Joshua Tree, California, U.S.A.	6.3	16.3	13	1.3	88	7.3	Hauksson *et al.* 1993
34	28.06.92	Big Bear, California, U.S.A.	6.7	23.5	10.5	2.2	80	7	Hauksson *et al.* 1993
		Reverse-slip							
35	09.02.71	San Fernando, California, U.S.A.	6.6	17.5	14	1.3*	49	11	Heaton 1982
36	09.01.82	Miramichi, Canada	5.2	5	5	1.0	58	3	Wetmiller *et al.* 1984
37	02.05.83	Coalinga, California, U.S.A.	6.5	28	13.5	2.1	30	8	Stein & Ekström 1992
38	07.10.83	Goodnow, New York, U.S.A.	5.1 (M_l)	2.2	2	1.1	74	7.8	Nábělek & Suárez 1989
39	04.08.85	Kettleman Hills, California, U.S.A.	5.9	19	8.7	2.2	12	7	Stein & Ekström 1992
40	05.10.85	Nahanni, Canada	6.6	31	16	1.9	30	14	Wetmiller *et al.* 1988
41	01.10.87	Whittier Narrows, California, U.S.A.	5.9	5	6	0.8	25	13	Hauksson & Jones 1989
42	22.01.88	Tennant Creek, Australia	6.3	13	10	1.3*	38	4	Bowman *et al.* 1990
43	22.01.88	Tennant Creek, Australia	6.7	19	10.5	1.8*	45	4.5	Bowman *et al.* 1990
44	28.06.91	Sierra Madre, California, U.S.A.	5.1	5.5	5	1.1	50	11.5	Hauksson 1991
		Oblique-slip							
45	16.10.70	Akita, Japan	6.0	14.5	11	1.3	—	—	Purcaru & Berckhemer 1982
46	08.05.74	Izu-Oki, Japan	6.8	19	9.5	2.0	—	—	Purcaru & Berckhemer 1982
47	01.08.75	Oroville, California, U.S.A.	5.6	10	9.5	1.1*	57	7.5	Fletcher *et al.* 1984
48	20.06.78	Thessaloniki, Greece	6.5	26.5	14.5	1.8*	80	—	Papazachos *et al.* 1979
49	13.08.78	Santa Barbara, California, U.S.A.	5.6	10	5	2.0	26	12	Corbett & Johnson 1982
50	22.12.83	Guinea, West Africa	6.3	25	13	1.9*	62	9	Langer *et al.* 1987b
51	10.07.84	North Wales, U.K.	4.7	3.5	4.1	0.9	87	21.5	Marrow & Walker 1988
52	21.03.86	Prince George, BC, Canada	5.2	7.5	7.5	1.0	52	12.5	Rogers *et al.* 1990
53	22.01.88	Tennant Creek, Australia	6.4	13	9	1.4*	50	4.5	Bowman *et al.* 1990
54	25.03.93	Scotts Mills, Oregon, U.S.A.	5.4	6.7	8.5	0.8	59	12	Crosson *et al.* 1994

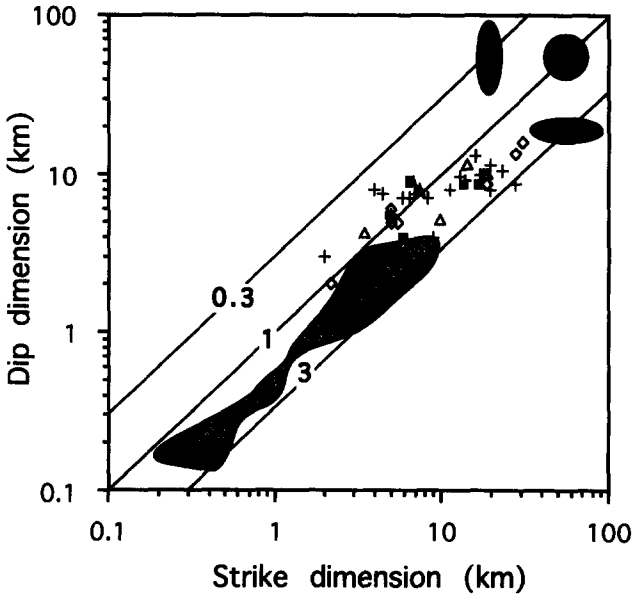

Fig. 4. Dip dimension vs strike dimension for 40 main-shock slip-surfaces as defined by aftershock loci, for normal dip-slip (filled squares), strike-slip (crosses), reverse dip-slip (open diamonds) and oblique-slip (open triangles) slip-surfaces associated with moderate magnitude (M = 4.2–6.8) events. Data sources are listed in Table 2. The field of nominal unrestricted faults in Fig. 3 is shown stippled. Straight lines correspond to aspect ratios of 0.3, 1.0 and 3.0.

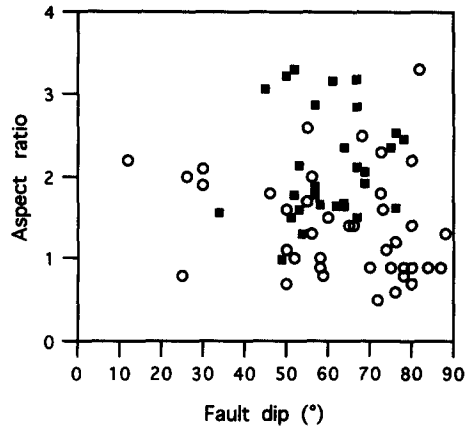

Fig. 5. Aspect ratio vs dip for unrestricted fault surfaces (filled squares) and earthquake main-shock slip-surfaces (open circles). Earthquake data sources are listed in Table 2.

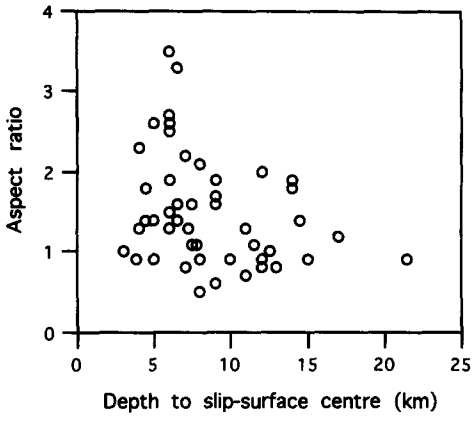

Fig. 6. Aspect ratio vs depth to the centre, for all earthquake slip-surfaces in Table 2.

cannot be identified with certainty and therefore have not been excluded. The available data strongly suggest that at least three of the strike-slip slip-surfaces with aspect ratios <1.0 are laterally restricted. Inclusion of laterally restricted slip-surfaces could be responsible for the low mean aspect ratio relative to that for the faults. For example, seismic events may be restricted to a single segment of a discontinuous neotectonic fault (e.g. Segall & Pollard 1980, Wesnousky 1988) and inclusion of such segments in the data set would reduce the slip-surface mean aspect ratio.

The earthquake slip-surface data demonstrate that slip directions are not the dominant control on the alignments of either the major axes of seismic slip-surfaces or of the fault surfaces on which they occur. Slip-surfaces of non-characteristic earthquakes (i.e. slip events that affect only a part of the fault surface on which they occur) will generally have the same alignments as the fault surfaces on which they occur. Segmented faults, however, may have slip-surfaces restricted to individual segments which will therefore differ in shape from that of the entire fault surface. By inference, the cumulative slip directions of inactive fault surfaces have not been the dominant control on the alignments of their major axes. There is no correlation of aspect ratios with the dips of either fault surfaces or earthquake main-shock slip-surfaces (Fig. 5) although a shallower angle of incidence with layer boundaries might be expected to enhance the crack-stopping effects of mechanical anisotropies. More examples of faults with dips <45° would be required to test this possibility. No relationship is apparent between the depths and aspect ratios of earthquake slip-surfaces (Fig. 6).

Role of mechanical anisotropy

Having eliminated the possibility of a positive relationship between slip direction and fault surface alignment the dominant control is likely to be mechanical anisotropy of the faulted volumes arising from their sub-horizontal layering. However, the mechanism by which up-dip and down-dip propagation is retarded relative to lateral propagation is uncertain. Displacement gradients are expected to increase with decrease in shear modulus (Walsh & Watterson 1988), i.e. for a given maximum displacement the fault dimensions will be less for a fault in shale than in sandstone. The rate of advance of a tip-line which is sub-parallel to layering will therefore be determined by the 'averaged' properties of the sequence. Rates of propagation of lateral tip-lines, on the other hand, will be determined by the rate of propagation in sandstone so long as it represents an appreciable proportion of the sequence. If the averaged mechanical properties are the principal control on fault shape, then the scale of the layering is unimportant so long as it is small in relation to the fault dimensions. Alternatively, the boundaries between layers of different properties could play an active role. If the layer furthest from the fault centre is more ductile, e.g. shales or salt in sedi-

mentary sequences (Rippon 1985a, Vendeville & Jackson 1992), crack propagation will be retarded at the boundary of such a layer by dissipation of crack tip stresses by ductile flow, i.e. by effective reduction of the stress intensity factor for both screw and edge dislocation regions of the tip-line. Tip-lines propagating laterally through horizontally layered sequences do not encounter ductility changes and their overall rate of advance is controlled by those parts of the tip-line propagating through the least ductile layers. Crack propagation asymmetry is commonly observed in layered materials, with laminated glass an extreme example. If layer boundaries play an active role as crack-stoppers then the frequency of the boundaries will be of equal, or greater, significance than the average properties of the sequence and the scale of the layering will assume a greater significance.

Whatever the precise mechanism by which layering influences fault surface shape it must operate not only on the well-defined repetitive layering typical of sedimentary sequences but also on the larger scale and less well-defined non-repetitive layering of the seismogenic layer.

If fault aspect ratios are strongly influenced by the mechanical layering of faulted volumes to the extent we suggest, then faults within highly anisotropic sequences will have higher aspect ratios than those in mechanically isotropic rocks. Such dependence of fault shape on anisotropy is consistent with our fault data. The relatively low aspect ratios of Gulf Coast faults (Table 1), illustrated by the near equidimensional fault surface shown in Fig. 1, are consistent with the relative homogeneity of this sand dominated sequence (sand/shale ratio $\geq$4:1) compared with sequences (sand/shale ratios 1:3–1.5:1) in the three other regions from which the fault data are derived.

However, the shape and alignment of fault surfaces in mechanically isotropic rocks is still not known. Dislocation theory suggests that the equilibrium form of a dislocation loop bounding a glide plane in a crystal is elongate parallel to the Burgers vector, or slip direction, on the grounds that the edge dislocation segments of the dislocation loop absorb more energy per unit length than screw dislocation segments (Nabarro 1967, Hull & Bacon 1984). The dislocation loop therefore tends to have greater length of screw dislocation than edge dislocation and has an aspect ratio $\approx(1 - \nu)$, where ν is Poisson's ratio. Typical values for Poisson's ratio are 0.1–0.4 (Price 1966, Table 1) and on this basis we would expect fault surface aspect ratios of *ca* 0.6–0.9 in homogeneous rocks, i.e. with fault surfaces elongate in the slip direction. These estimates are consistent with the experimental data of Lockner *et al.* (1991) who used acoustic emission locations to track shear crack growth in a specimen of homogeneous granite, and determined that tip-lines advanced more rapidly in the shear direction, i.e. the crack form was elongate parallel to the slip direction.

Our results show that no matter what the intrinsic asymmetry and alignment of a slip-surface in isotropic materials, they are usually outweighed in layered sequences by the effects of mechanical anisotropy. In particular normal faults are characterized by sub-horizontal major axes parallel to sequence layering but perpendicular to the fault slip direction. Mode I fractures, which have uniform energy absorption around the tip-line and therefore are likely to be circular in a homogeneous medium, are also elliptical in layered rocks with an average aspect ratio of *ca* 2 (Petit *et al.* 1994). If the aspect ratio of faults and fractures is mainly a consequence of mechanical anisotropy, the question arises as to why there is such a limited range of observed aspect ratios, or specifically, why do we not see faults with higher aspect ratios? Petit *et al.* (1994) have observed ratios of up to *ca* 77 for mode I fractures confined to individual sandstone beds and we think it likely that faults of high aspect ratio also exist but are not included in our data set. The most extreme aspect ratios are likely to be on faults restricted to a single competent layer bounded by thick and/or very incompetent layers, as in the fault illustrated in Fig. 7. This normal fault, which has some features in common with boudinage (e.g. spaced heterogeneous extension structures confined to a competent layer bounded by two incompetent layers), is mainly within two chalk units and terminates upwards and downwards in thin clay layers. The fault terminations are accommodated by very high displacement gradients (*ca* 1) which in turn are accommodated by plastic flow with substantial thickening and thinning of the clay layers (Fig. 7). In general such extreme competence contrasts are most likely to occur on the scale of single bedding units as thicker intervals tend to 'average' mechanical properties, which is one reason why boudinage is rarely observed in layers more than 20–30 m thick. Throw strike-projections are not generally available for small faults in the scale range which we would expect to be characterized by a much wider range of aspect ratios than is observed for larger faults.

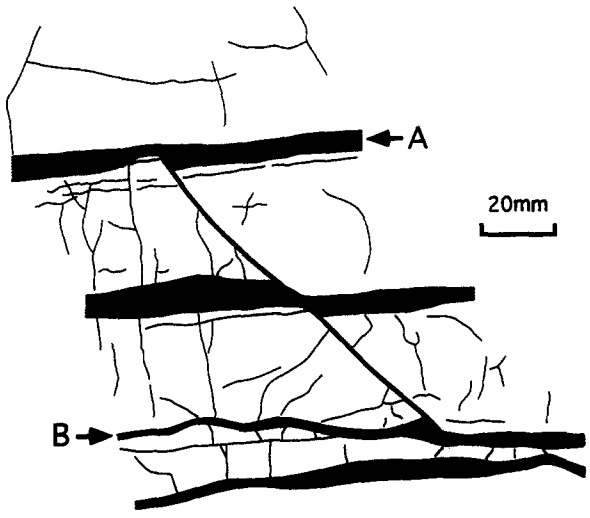

Fig. 7. Outcrop (Flamborough Head, U.K.) of a small fault in chalk (dip dimension 11 cm) vertically restricted between the two clay layers, labelled A and B. Fault terminations within the clay layers are accommodated by plastic flow giving rise to substantial thickness variations (*ca* 200–250%) within the clay layers across the fault.

Further questions, primarily concerning scale effects,

arise from our conclusions regarding the role of mechanical anisotropy in determining fault shape. For example, can either the layering or the layer boundaries within the seismogenic layer be directly compared with those within a sedimentary sequence? Furthermore, our conclusion requires not only a limited range of mechanical properties but that this range occurs over a wide range of scales. Could the scale of anisotropy responsible for an aspect ratio of two on a fault with a dip dimension of 100 m have a similar effect on a fault surface with a dip dimension of 10 km or would the layering need to be on a correspondingly larger scale? Few data are available on mechanical anistropy within the middle and lower seismogenic layer so answers to these questions cannot be given with confidence.

SHAPE AND ALIGNMENT OF RESTRICTED NORMAL FAULT SURFACES

Restricted faults are distinguished primarily by locally higher displacement gradients adjacent to tip-lines and also by significant departures from elliptical tip-lines. Restricted faults therefore have locally more closely spaced throw contours, lower overall symmetries and a wider range of aspect ratios than unrestricted faults. Figures 8–11 illustrate the variety of fault shapes which may result from restricted fault growth.

The shapes of laterally and vertically restricted faults are clearly differentiated on a plot of dip dimension vs strike dimension (Fig. 12). Restricted faults generally plot outside the data field for unrestricted faults, and aspect ratios range from 0.5 to 1.8 (mean *ca* 1.0) for laterally restricted faults and from 1.8 to 8.4 (mean *ca* 3.5) for vertically restricted faults. The data distribution in Fig. 12 is continuous; with increasing restriction of a fault surface in one direction its aspect ratio increasingly departs from the mean unrestricted value (~2). Aspect ratios <1.3 are generally associated with laterally restricted faults, and values of >2.5 with vertically restricted faults (Fig. 12).

Normalized radial throw profiles for unrestricted faults show a near-linear decrease in throw from fault centre to tip-line (Figs 2c i and 13c). By contrast, radial throw profiles for restricted faults either show a non-linear profile with abrupt steepening of the throw gradient towards the restricted tip-point (Fig. 2c ii) or, where the effects of restriction extend to the fault centre, a marked difference between throw gradients on either side of the fault centre (Fig. 2c iii). Figure 13(d) includes profiles of both types. As would be expected laterally restricted faults generally have lower ratios of fault strike dimension to maximum displacement than unrestricted faults of similar maximum displacement (compare Figs 13a & b).

These characteristics are all expressions of a single feature of restricted faults, namely the relatively high throw gradients in the vicinity of restricted tip-lines (see also Peacock & Sanderson 1991). As only two-dimensional data are available in many cases locally high

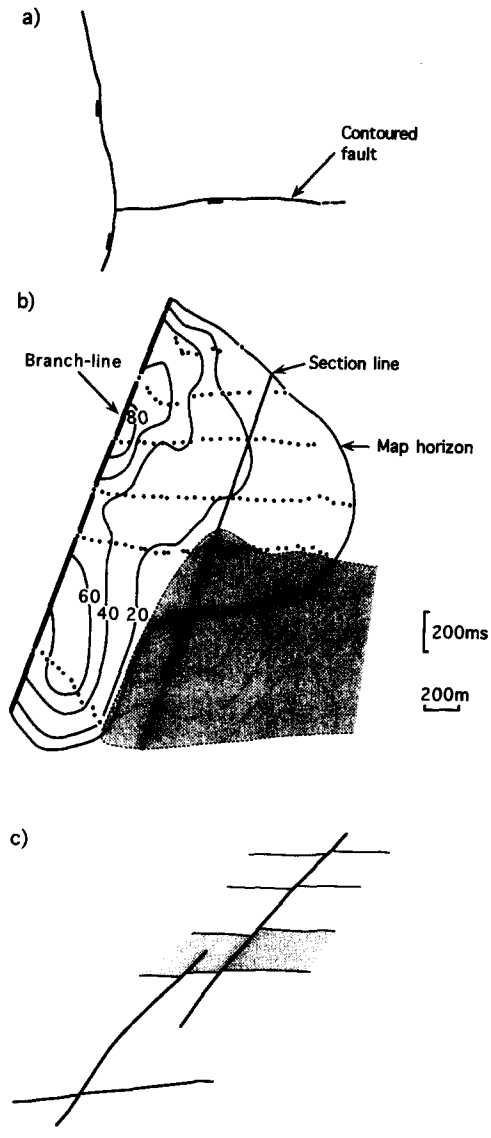

Fig. 8. (a) Map, (b) throw contour diagram and (c) cross-section for a syn-sedimentary normal fault from the Timor Sea. Horizon A is the base of the syn-faulting sequence above which high throw gradients are reflected in relatively straight and closely spaced throw contours. This fault is vertically and laterally restricted by adjacent overlapping faults (one of which is shown stippled in (b) and on the cross-section (c)) and has an irregular shape which departs significantly from that of the ideal elliptical fault. Fault maximum throw is 27 ms (*ca* 41 m), strike dimension is *ca* 2.5 km and the aspect ratio *ca* 1.4. Vertical and horizontal scales are approximately equal and are the same on all diagrams.

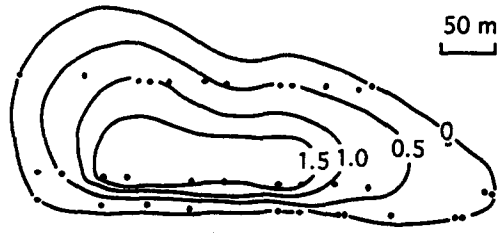

Fig. 9. Throw contour (m) diagram for a normal fault from the North Derbyshire Coal-field, modified from Fig. 3 of Rippon (1985a). The view is normal to the fault surface which has an aspect ratio of *ca* 2.7. Propagation of the lower tip-line of this fault is interpreted by Rippon to have been retarded by a thick sandstone bed. Vertical and horizontal scales are approximately equal.

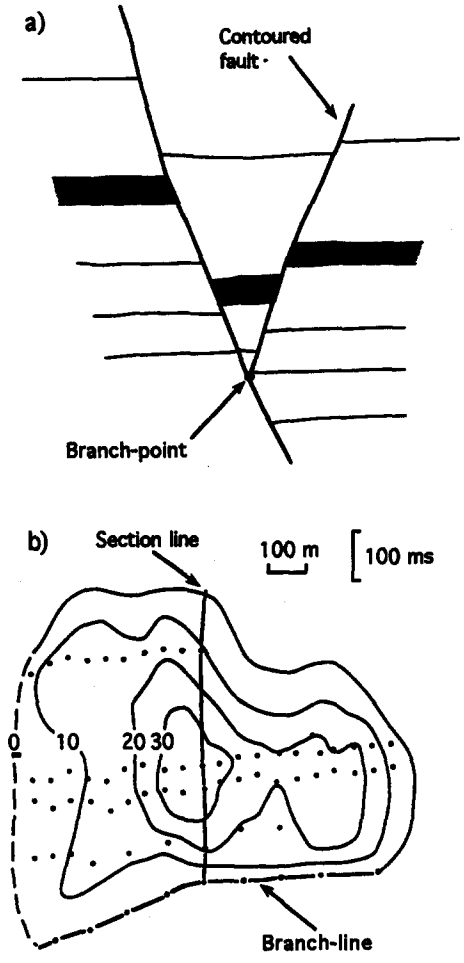

Fig. 10. (a) Cross-section and (b) throw contour diagram (viewed normal to the fault surface) for a seismically-imaged fault from the Timor Sea. The location of the cross-section is indicated on (b). The fault is antithetic to a larger fault which it intersects at a branch-point as shown in (a). This branch-point can be traced along strike as the branch-line shown in (b). Fault maximum throw is 37 ms (*ca* 56 m), strike dimension is *ca* 1 km and the aspect ratio *ca* 1.4. The dashed line in (b) indicates the approximate location of the left-hand lateral tip-line. Vertical and horizontal scales are approximately equal and are the same on each figure.

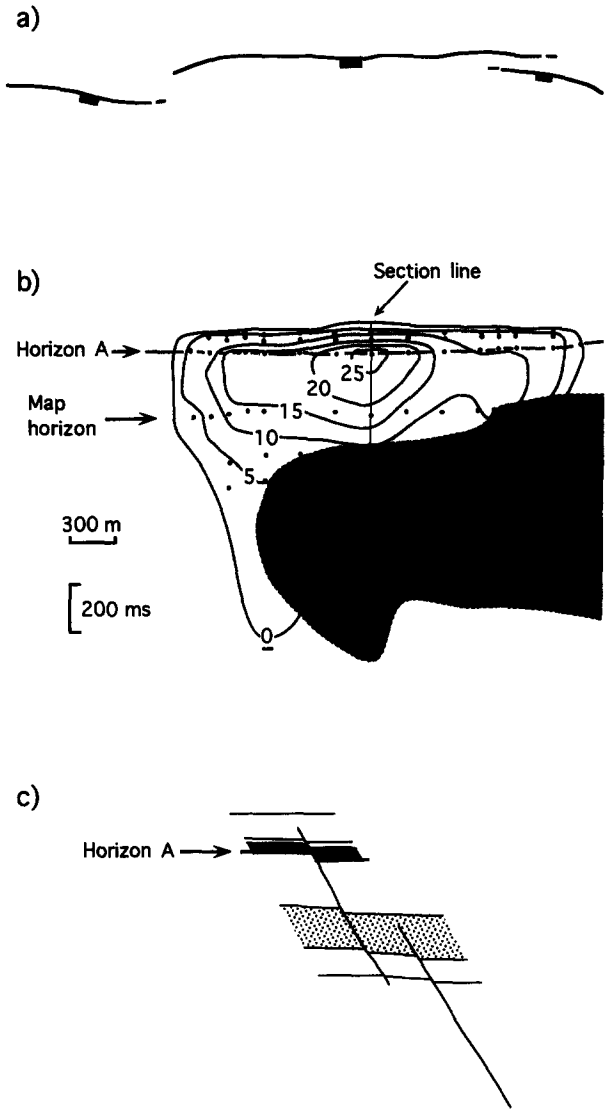

Fig. 11. (a) Map, (b) throw contour diagram and (c) cross-section for a seismically-imaged normal fault from the Gulf Coast. The contoured fault is laterally restricted by a contemporaneous orthogonal fault shown in (a) which it intersects along the steep branch-line shown in (b). The irregular shape of the lower right portion of the fault surface is due to a nearby fault, indicated by the stippled area in (b) and shown in the cross-section (c), which forms both lateral and dip overlaps with the contoured fault. Fault maximum throw is 85 ms (*ca* 106 m) and the aspect ratio is *ca* 0.64. Vertical and horizontal scales are approximately equal and are the same on each figure.

displacement gradients are often the clearest indication of restricted fault growth. In all cases the high gradient is a result of reduced tip-line propagation rate relative to the rate of increase in maximum displacement. In this respect the immediate causes of irregular fault surface forms are the same as those giving rise to the typical elliptical form of unrestricted faults. We know of no example in which irregularity of a fault surface is associated with a relatively low displacement gradient arising from relatively rapid propagation of a tip-line. Although all examples of restricted fault growth are ultimately due to a reduction in the relative rate of tip-line propagation this has a variety of causes, which are considered below.

We do not consider here fault surface asymmetries associated either with unconformities or with fault reactivation, or with both. Neither do we consider the apparent asymmetries of crustal scale faults which intersect the base of the seismogenic layer.

Restriction by free surface and lithological effects

A fault intersecting a free surface has been assumed to have a maximum displacement at or near the initial free surface (Barnett *et al.* 1987); this implies that the surface trace of an active fault corresponds to the maximum dimension of the fault. Figure 8 shows the restricted upper tip-line and closely spaced throw contours of a syn-sedimentary fault in which the maximum displacement occurs at the initial free surface (Petersen *et al.* 1992, Childs *et al.* 1993). Throws recorded within the syn-faulting sequence are limited to the component of throw which post-dated successively younger syn-faulting horizons. The form and spacing of the throw contours above the initial free surface are then functions

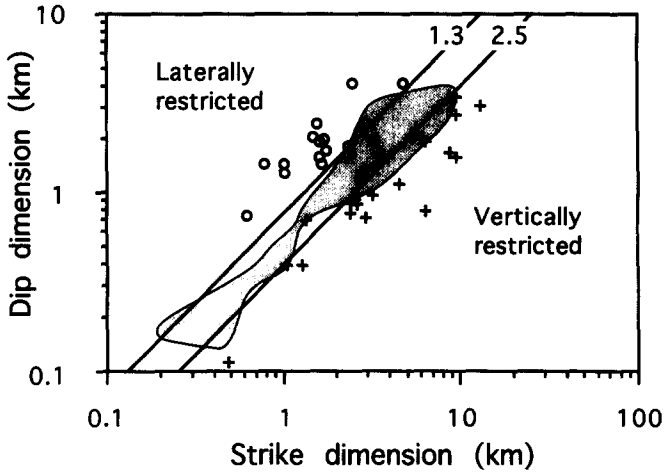

Fig. 12. Dip dimension vs strike dimension for 39 laterally (open circles) and vertically (crosses) restricted faults from the four regions listed in Table 1. Stippled area is the field of unrestricted faults from Fig. 3. Straight lines show aspect ratios of 1.3 and 2.5. Faults with aspect ratios of <1.3 are commonly laterally restricted and those with aspect ratios of >2.5 are frequently vertically restricted.

of the relative rates of fault throw and of sedimentation. When the rate is low relative to the rate of throw, the throw contours are more closely spaced and approximately horizontal. Many syn-sedimentary faults have throw contour patterns broadly consistent with this model (Clausen *et al.* 1993, Childs *et al.* 1995). We observe that earthquake slip-surfaces that intersect the free surface generally have higher aspect ratios than do blind slip-surfaces, consistent with the maximum displacements on syn-sedimentary faults lying at or close to the pre-faulting free surface. However, as the maximum seismic slips on some seismic slip-surfaces which intersect the free surface lie in the sub-surface, the surface traces do not correspond to the maximum dimensions in these cases (Wells & Coppersmith 1994). We conclude therefore that the maximum displacements on syn-sedimentary faults also may not always be at the initial free surface and in such cases the contour patterns may differ from that shown in Fig. 8.

As previously discussed, lithological layering gives rise to elliptical fault surfaces. However, where the thicknesses of lithological layers are large relative to the fault dimension or where the contrast in layer properties is particularly marked, propagation of a tip-line at a layer boundary may be restricted to such a degree that an overall elliptical tip-line form is not maintained. A rectangular tip-line loop would be expected for the fault illustrated in Fig. 7 and a less extreme example is the fault illustrated in Fig. 9 (fig. 3 of Rippon 1985a) which has an almost straight lower tip-line that Rippon (1985a) suggests was possibly arrested at the junction between the Piper coal seam and an unusually thick sandstone below (see also Burgmann *et al.* 1994). In addition to the distinctive shape of the tip-line this fault also has higher throw gradients close to the lower tip-line and an aspect ratio (*ca* 2.7) higher than the average for unrestricted coal-field faults. This fault is believed to exemplify a process which occurs on a wide range of scales.

Confinement by interaction with other faults

Growth of a fault can be modified by interaction either with a contemporaneous fault or with an earlier fault. The growth of contemporaneous faults is affected from the time that their elastic strain fields overlap, which may occur well before the surfaces intersect one another. The best documented examples of this type of interaction are those at lateral overlaps, or relay zones, between synthetic fault surfaces (Morley *et al.* 1990, Walsh & Watterson 1990, Peacock 1991, Peacock & Sanderson 1994, Trudgill & Cartwright 1994, Childs *et al.* 1995, Huggins *et al.* 1995). The distance over which there is interaction between two faults, i.e. across a relay zone or where faults intersect, generally increases with increase in fault displacement. The maximum ratios between distance separating interacting faults and fault throw appears often to lie in the range 3–10:1 (average 5:1); distance is taken as distance to the other fault from the point on a fault trace where throws begin to decrease rapidly.

High displacement gradients which characterize fault surfaces bounding relay zones (Figs. 2b & c) are due to a mutual retardation of the propagating tips of the two faults, giving rise to modifications of fault surface ellipses of the type illustrated in Figs. 14(b) & (d). Interaction is most marked where a fault surface intersects a contemporary fault along a branch line, or an earlier fault along an intersection line. In each case the tip-line loop is incomplete and the fault boundary is a loop including a relatively straight branch-line or intersection line (Fig. 11). Where a fault terminates at a branch-line the throw contours may either be locally sub-parallel to the branch-line along which the throw is low or zero, as in Fig. 10, or be at a high angle to the branch line with a maximum throw on or adjacent to the branch line, as in Fig. 11.

Figures 8, 10 and 11 illustrate normal faults which are restricted in a number of different ways and at varying locations around the tip-line. The fault in Fig. 8 is restricted not only by both lateral and vertical overlaps with nearby faults but also by the free surface. The combination of vertical and lateral restriction is reflected in the rectangular shape of the upper left-hand part of the fault surface and by the convex-upwards tip-line along the lower right-hand part of the fault. The antithetic fault in Fig. 10 terminates downwards at a sub-horizontal branch-line to which throw contours are locally parallel, but the maximum throw is located centrally which is consistent with nucleation of the fault at some distance from the branch-line. By contrast, Fig. 11 shows a fault bounded laterally by a steeply-inclined branch-line along which the maximum throw occurs. In addition, the form of the fault surface in Fig. 11 is strongly affected by the proximity of a second fault surface (stippled) which overlaps both laterally and vertically. The relationships illustrated are not exclusive, and many faults will be restricted in more than one direction and by more than one process. In such cases fault shapes and throw patterns may be highly irregular.

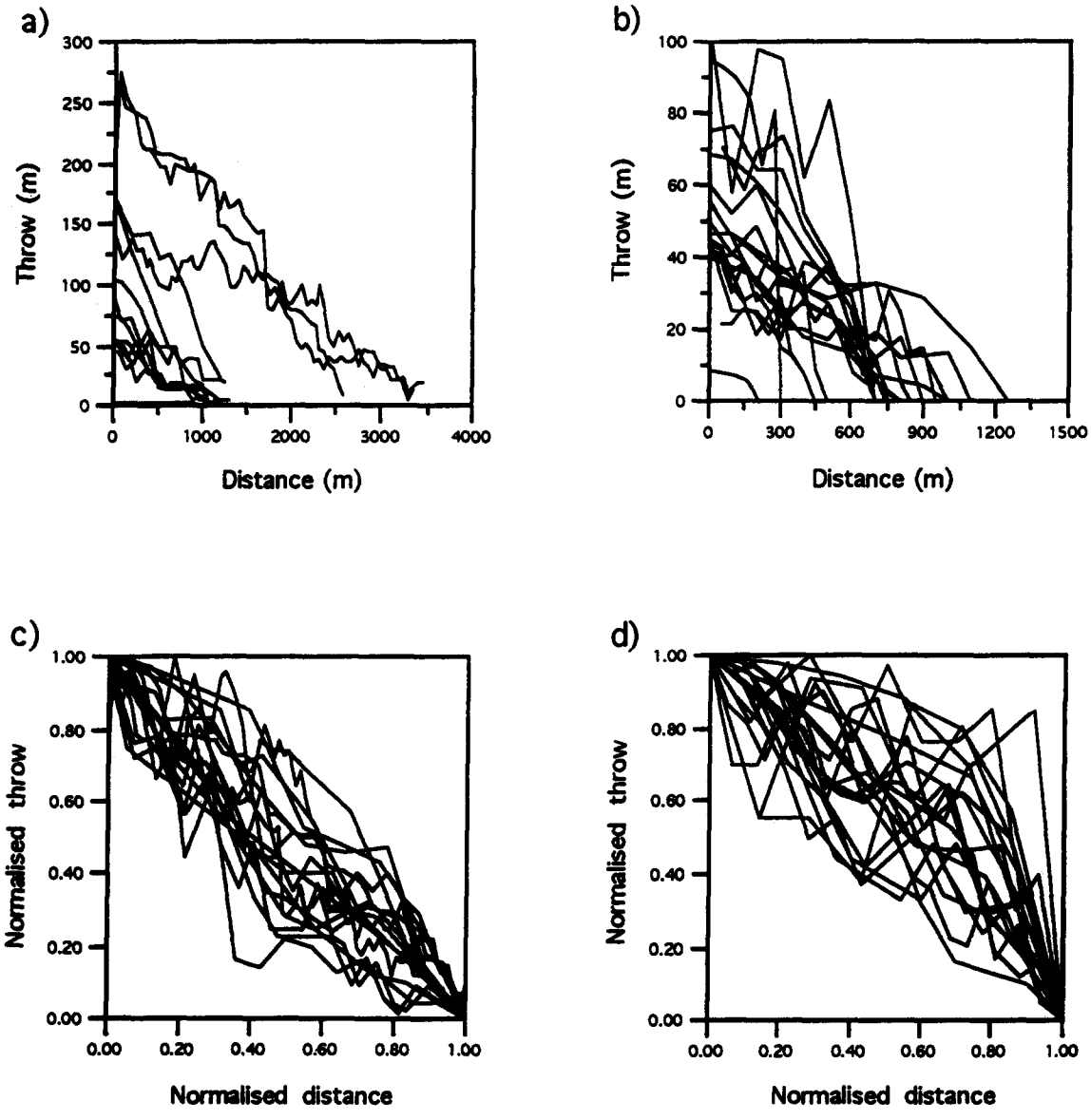

Fig. 13. Horizontal profiles of throw vs distance from the point of maximum throw for (a) unrestricted and (b) restricted faults. (c) and (d) are the normalized equivalents of (a) and (b), respectively, with data normalized to maximum fault throw and distance to fault tip. Profiles defined by less than six throw observations and with minimum observed throws of >15% of the maximum are excluded. The small wavelength throw variations are due to errors related to data resolution.

Faults exhibiting multiple restriction (e.g. Figs. 8 and 11) are both frequent and widespread. Figure 14 schematically illustrates fault surface shapes and displacement patterns corresponding to the different types of restriction noted.

FAULT INTERACTIONS

Significance of fault restriction

We would expect higher proportions of unrestricted faults in low density immature fault systems and interactions with other faults to increase with increases in both density and sizes of faults. We have examined an array of near parallel-striking normal faults in a 100 km^2 area of the Timor Sea in which complexities due to cross-faults are minimal. Discussion is confined to lateral restriction because of the depth limitations of the seismic data. Tip-points were classified as restricted or unrestricted on the basis of the criteria described (Fig. 2c). Of the 49 fault traces with both tip-points shown on a Base Miocene horizon map, only 2% have both tip-points unrestricted, 27% have one tip-point unrestricted and both tip-points are restricted on 71%. The fault trace density of this map is 1.47 km km^{-2} at a throw truncation of *ca* 10 m, which is not an unusually high density for seismically-imaged faults. Given these proportions in a relatively immature fault system, more generally fault surfaces approximating to regular ellipses will be exceptional.

Fault growth by linkage

It might be expected that as a parallel fault system matures many neighbouring faults would intersect and merge (e.g. Peacock & Sanderson 1994, Cartwright *et al.* 1995, Childs *et al.* 1995), and that surfaces of such

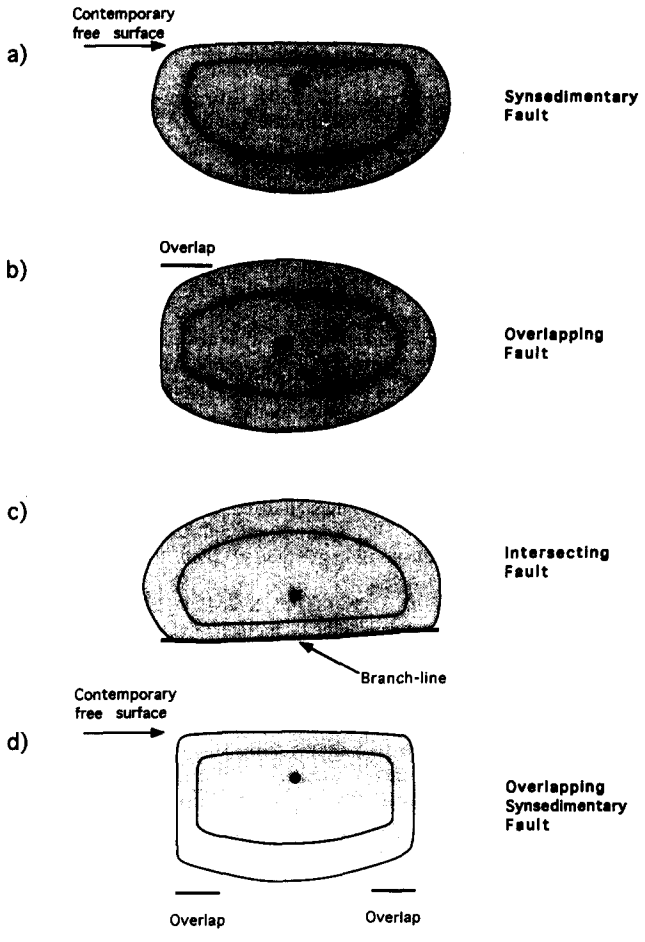

Fig. 14. Schematic diagram illustrating variations in fault surface shapes, displacement contour patterns and points of maximum displacement (filled circle) due to restriction by the free surface (a & d) and/or by adjacent faults (b, c & d). In each case the view is normal to the fault surface (stippled).

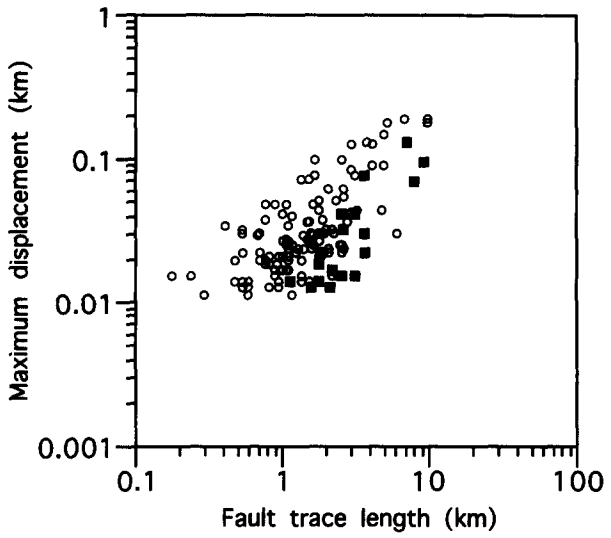

Fig. 15. Maximum displacement vs nominal trace length for laterally unrestricted (filled squares) and laterally restricted (open circles) faults for a three-dimensional seismic data set from the Timor Sea. Data are from a single pre-faulting horizon. The seismic shotline spacing is 125 m. Faults imaged on less than three lines and/or with throws <10 m (approximately equal to the throw resolution) were excluded, as also were faults with maximum displacements beyond the mapped area. Nominal trace lengths were calculated by doubling the distances from fault tips to the maximum displacements. Arrays of fault segments which could be traced vertically to a single structure were treated as a single fault. Data for 20 unrestricted and 147 restricted faults are shown.

merged faults would have distinctive non-elliptical forms with two throw maxima. But faults which obviously have resulted from merging of two antecendent faults appear to be relatively uncommon. When two faults grow laterally towards one another they interact before intersecting because of the interference between their respective elastic strain fields which extends beyond the tip-points. High displacement gradients therefore characterize both of the faults prior to their intersection, thus reducing their aspect ratios to a value which is probably significantly less than 2. When the two faults merge the aspect ratio of the merged fault is likely to be <4.0 and will reduce as the merged fault continues to grow as a single unit. The complex throw contour patterns expected in a recently merged fault are unlikely to persist recognisably after significant further fault growth (see also Anders & Schlische 1994).

Relationships between fault displacement and dimensions

Our data suggest that interaction between faults has significant effects on data relating fault dimensions to displacements (see also Cartwright *et al.* 1995). Figure 15 is a plot of maximum displacement vs trace length for traces of laterally unrestricted and laterally restricted faults from the Timor Sea data set and shows that, for a given displacement, unrestricted faults generally have greater trace lengths than restricted faults. Slopes of best-fit lines for both types of fault are similar and in the range 1.0–1.5 so restriction of fault growth by interaction with adjacent faults appears not to affect the power-law exponent (n) of the displacement–trace length equation (i.e. $D = aL^n$, D = maximum displacement and L = trace length), but does increase the value of the variable, a, as was suggested by Gillespie *et al.* (1992). When tip-line propagation is retarded the maximum displacement increases more quickly relative to the increase in the fault-trace length, diverting the steeper fault growth path above the unrestricted growth line, as shown in Fig. 16. The modelled growth paths shown in Fig. 16 are consistent with the Timor Sea data in Fig. 15.

CONCLUSIONS

Blind isolated normal faults in layered sequences have average aspect ratios 2.15, with sub-horizontal major axes. Slip-surface aspect ratios for strike-slip, oblique-slip and dip-slip earthquake main-shock slip-surfaces range from 0.5 to 3.5 and long axis alignments are independent of slip type. The principal control on the shape of these unrestricted faults is therefore inferred to be mechanical anisotropy associated with lithological layering, which retards layer-normal tip-line propagation and results in layer-parallel alignment of the fault surface ellipse.

The growth of most faults (all seismically resolvable

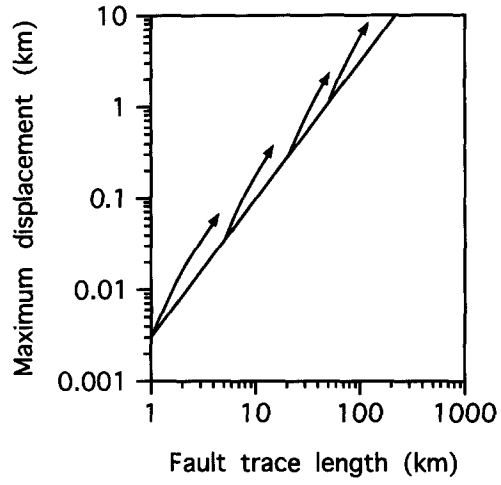

Fig. 16. Model growth curves for four faults restricted at trace lengths of 1, 5, 20 and 50 km by high-angle intersection with a second fault. Prior to intersection the faults growth relationship was $D = 0.003L^{1.5}$, where D = maximum displacement and L = trace length. After intersection propagation of one fault tip was arrested and the displacement–trace length relationship changed to $D = 0.003L^{1.5}/2 + 0.5l$, where l = fault trace length at time of intersection.

faults in the Timor Sea data set) is restricted either by the free surface and/or by neighbouring faults. These restricted faults have aspect ratios ranging from 0.5 to 8.4; aspect ratios of <1.3 are commonly observed for laterally restricted faults and values of >2.5 for vertically restricted faults. Restriction of fault growth in a given direction results in reduced curvature of the tip-line and of displacement contours, positioning of the maximum displacement closer to the restricted fault tip-line and an increase in throw gradients towards the restricted margin. Locally high displacement gradients, easily detected on two-dimensional throw profiles, often provide the clearest indication of restricted fault growth. Many faults are restricted at several places on the tip-line loop and these faults are often characterized by highly irregular shapes and displacement patterns.

Because fault interaction results in increased displacement gradients, subsequent fault linkage is unlikely to produce aspect ratios beyond the normal range for unrestricted faults. Lateral fault interaction produces an increase in the ratio of maximum displacement to trace length, but appears not to change the power-law exponent of the entire population.

Acknowledgements—This research was part funded by the OSO/NERC Hydrocarbon Reservoirs LINK Programme (project 827/7053). We thank several oil companies for providing seismic data and Fault Analysis Group colleagues for discussions on many aspects of this work. We are grateful to Marie Eeles, Dan Ellis and Jenny Procter for preparation of diagrams. Thanks are also due to Joe Cartwright and Rob Knipe for their constructive reviews. Badley Earth Sciences FAPS software was used for correlation, projection and analysis of fault data.

REFERENCES

Abe, K. 1974, Fault parameters determined by near- and far-field data: the Wasaka Bay earthquake of March 26 1963. *Bull. seism. Soc. Am.* **64**, 1369–1382.

Allen, C. R., Clayton, C. R. & Hauksson, E. 1990. Partial support of joint USGS-CALTECH southern California seismographic network. United States Geological Survey, Summaries of Technical Reports.

Anders, M. H. & Schlische, R. W. 1994. Overlapping faults, intrabasin highs and the growth of normal faults. *J. Geol.* **102**, 165–180.

Arabasz, W. J., Richins, W. D. & Langer, C. I. 1981. The Pocatello Valley (Idaho–Utah border) earthquake sequence of March to April 1975. *Bull. seism. Soc. Am.* **71**, 803–826.

Bakun, W. H., Clark, M. M., Cockerham, R. S., Ellsworth, W. L. Lindh, A. G., Prescott, W. H., Shakal, A. F. & Spudich, P. 1984. The 1984 Morgan Hill, California, earthquake. *Science* **225**, 288–291.

Barnett, J. A. M., Mortimer, J., Rippon, J., Walsh, J. J. & Watterson, J. 1987. Displacement geometry in the volume containing a single normal fault. *Bull. Am. Ass. Petrol. Geol.* **71**, 925–937.

Bounif, A., Haessler, H. & Meghraoui, M. 1987. The Constantine (northeast Algeria) earthquake of October 27, 1985: surface ruptures and aftershock study. *Earth Planet. Sci. Lett.* **85**, 451–460.

Bowman, J. R., Gibson, G. & Jones, T. 1990. Aftershocks of the 1988 January 22 Tennant Creek, Australia intraplate earthquakes: evidence for a complex thrust-fault geometry. *Geophys. J. Int.* **100**, 87–97.

Burgmann, R., Pollard, D. D. & Martel, S. J. 1994. Slip distributions on faults: effects of stress gradients, inelastic deformation, heterogeneous host-rock stiffness, and fault interaction. *J. Struct. Geol.* **16**, 1675–1690.

Cartwright, J. A., Trudgill, B. & Mansfield, C. S. 1995. Fault growth by segment linkage: an explanation for scatter in maximum displacement and trace length data from the Canyonlands Grabens of S.E. Utah. *J. Struct. Geol.* **17**, 1319–1326.

Childs, C., Easton, S. J., Vendeville, B. C., Jackson, M. P. A., Lin, S. T., Walsh, J. J. & Watterson, J. 1993. Kinematic analysis of faults in a physical model of growth faulting above a viscous salt analogue. *Tectonophysics* **228**, 313–329.

Childs, C., Watterson, J. & Walsh, J. J. 1995. Fault overlap zones within developing normal fault systems. *J. geol. Soc. Lond.* **152**, 535–549.

Clausen, O.-R., Korstgard, J. A., Petersen, K., McCann, T., O'Reilly, B. M., Shannon, P. M., Howard, C. B., Mason, P. J., Walsh, J. J. & Watterson, J. 1994. Systematics of faults and fault arrays. In: *Modelling the Earth for Oil Exploration* (edited by Helbig, K.). Elsevier, Amsterdam, 205–316.

Corbett, E. J. & Johnson, C. E. 1982. The Santa Barbara, California, earthquake of 13 August 1978. *Bull. seism. Soc. Am.* **72**, 2201–2226.

Crosson, R. S., Malone, S. D., Qamar, A. I. & Ludwin, R. S. 1994. Washington Regional Seismograph Network Operations. United States Geological Survey, Summaries of technical reports.

Dawers, N. H. & Anders, M. H. 1995. Displacement–length scaling and fault linkage. *J. Struct. Geol.* **17**, 607–614.

Eaton, J. P., O'Neill, M. E. & Murdock, J. N. 1970. Aftershocks of the 1966. Parkfield-Cholame, California, earthquake: a detailed study. *Bull. seism. Soc. Am.* **60**, 1151–1197.

Fletcher, J., Boatwright, J., Haar, L., Hanks, T. & McCarr, A. 1984. Source parameters for aftershocks of the Oroville, California, Earthquake. *Bull. seism. Soc. Am.* **74**, 1101–1123.

Gagnepain-Beyneix, J., Haessler, H. & Modiano, T. 1982. The Pyrenean earthquake of February 29, 1980: an example of complex faulting. *Tectonophysics* **85**, 291–312.

Gillespie, P. A., Walsh, J. J. & Watterson, J. 1992. Limitations of dimension and displacement data from single faults and the consequences for data analysis and interpretation. *J. Struct. Geol.* **14**, 1157–1172.

Grant, W. C., Weaver, C. S. & Zollweg, J. E. 1984. The 14 February 1981 Elk Lake, Washington, earthquake sequence. *Bull. seism. Soc. Am.* **74**, 1289–1309.

Haessler, H., Gaulon, R., Rivera, L., Console, R., Frogneux, M., Gaspirini, G., Martel, L. G. P., Siciliano, M. & Cisternas, A. 1988. The Perugia (Italy) earthquake of 29 April 1984: A microearthquake survey. *Bull. seism. Soc. Am.* **78**, 1948–1964.

Haessler, H., Hoang-Trong, P., Schick, R., Schneider, G. & Strobach, K. 1980. The September 3, 1978, Swabian Jura earthquake. *Tectonophysics* **68**, 1–14.

Harlow, D. H., White, R. A., Rymer, M. J. & Alvarez, S. G. 1993. The San Salvador earthquake of 10 October 1986 and its historical context. *Bull. seism. Soc. Am.* **83**, 1143–1154.

Huaksson, E. 1991. Analysis of earthquake data from the Greater Los Angeles Basin and adjacent offshore area, southern California.

United States Geological Survey, Summaries of Technical Reports.

Hauksson, E. & Jones, L. M. 1989. The 1987 Whittier Narrows earthquake sequence in Los Angeles, southern California: seismological and tectonic analysis. *J. geophys. Res.* **94**, 9569–9589.

Hauksson, E., Jones, L. M., Huttone, K. & Eberhart-Phillips, D. 1993. The 1992 Landers earthquake sequence: seismological observations. *J. geophys. Res.* **98**, 19,835–19,858.

Heaton, T. H. 1982. The 1971 San Fernando earthquake: a double event? *Bull. seism. Soc. Am.* **72**, 2037–2062.

Heaton, T. H. 1989. Southern California earthquake project. United States Geological Survey, Summaries of Technical Reports.

Herrmann, R. B., Langston, C. A. & Zollweg, J. E. 1982. The Sharpsburg, Kentucky, earthquake of 27 July 1980. *Bull. seism. Soc. Am.* **72**, 1219–1239.

Hull, D. & Bacon, D. J. 1984. *Introduction to Dislocations* (3rd edition). *International Series on Materials Science and Technology*, Vol. 37.

Huggins, P., Watterson, J., Walsh, J. J. & Childs, C. 1995. Relay zone geometry and displacement transfer between normal faults recorded in coal-mine plans. *J. Struct. Geol.* **17**, 1741–1755.

Ishida, M. 1984. Spatial-temporal variation of seismicity and spectrum of the 1980 earthquake swarm near the Izu Peninsula, Japan. *Bull. seism. Soc. Am.* **74**, 199–221.

Jones, L. M., Hutton, L. K., Given, D. D. & Allen, C. R. 1986. The North Palm Springs, California earthquake sequence of July 1986. *Bull. seism. Soc. Am.* **76**, 1830–1837.

Lahr, J. C., Page, R. A., Stephens, C. D. & Fogleman, K. A. 1986. Sutton, Alaska, earthquake of 1984: evidence for activity on the Talkeetna segment of the Castle Mountain fault system. *Bull. seism. Soc. Am.* **76**, 967–983.

Langer, C. J. & Bollinger, G. A. 1991. The southeastern Illinois earthquakes of 10 June 1987: The later aftershocks. *Bull. seism. Soc. Am.* **81**, 423–445.

Langer, C. J., Bollinger, G. A. & Merghelani, H. M. 1987a. Aftershocks of the 13 December 1982 North Yemen earthquake: conjugate normal faulting in an extensional setting. *Bull. seism. Soc. Am.* **77**, 2038–2055.

Langer, C. J., Bonilla, M. G. & Bollinger, G. A. 1987b. Aftershocks and surface faulting associated with the intraplate Guinea, West Africa, earthquake of 22 December 1983. *Bull. seism. Soc. Am.* **77**, 1579–1601.

Lockner, D. A., Byerlee, J. D., Kuksenko, V., Ponomarev, A. & Sidorin, A. 1991. Quasi-state fault growth and shear fracture energy in granite. *Nature* **350**, 39–42.

Lyon-Caen, H., Armijo, R., Drakopoulos, J., Baskoutass, J., Delibassis, N., Gaulon, R., Kouskouna, V., Latoussakis, J., Makropoulos, K., Papadimitriou, P., Papanastassiou, D. & Pedotti, G. 1988. The 1986 Kalamata (South Peloponnesus) earthquake: detailed study of a normal fault, evidences for east–west extension in the Hellenic arc. *J. geophys. Res.* **93**, 14,967–15,000.

Magistrale, H., Jones, L. & Kanamori, H. 1989. The Superstition Hills, California, earthquakes of 24 November 1987. *Bull. seism. Soc. Am.* **79**, 239–251

Marrett, R. & Allmendinger, R. W. 1991. Estimates of strain due to brittle faulting: sampling of fault populations. *J. Struct. Geol.* **13**, 735–738.

Marrow, P. C. & Walker, A. B. 1988. Lleyn earthquake of 1984 July 19: aftershock sequence and focal mechanism. *Geophys. J.* **92**, 487–493.

Mendoza, C. & Hartzell, S. H. 1988. Aftershock patterns and main shock faulting. *Bull. seism. Soc. Am.* **78**, 1438–1449.

Mezcua, J., Herraiz, M. & Buform, E. 1984. Study of the 6 June 1977 Lorca (Spain) earthquakes and its aftershock sequence. *Bull. seism. Soc. Am.* **74**, 167–179.

Morley, C. K., Nelson, R. A., Patton, T. L. & Munn, S. G. 1990. Transfer zones in the East African rift system and their relevance to hydrocarbon exploration in rifts. *Bull. seism. Soc. Am.* **74**, 1234–1253.

Nabarro, F. R. N. 1967. *Theory of Crystal Dislocations*. Clarendon Press, Oxford.

Nábêlek, J. & Suáraz, G. 1989. The 1983 Goodnow earthquake in the central Adirondacks, New York: rupture of a simple, circular crack. *Bull. seism. Soc. Am.* **79**, 1762–1777.

Pacheco, J. & Nábêlek, J. 1988. Source mechanisms of three moderate California earthquakes of July 1986. *Bull. seism. Soc. Am.* **78**, 1907–1929.

Papazachos, B., Mountrakis, D., Psilovikos, A. & Leventakis, G. 1979. Surface fault traces and fault plane solutions of the May–June 1978 major shocks in the Thessaloniki area, Greece. *Tectonophysics* **53**, 171–183.

Peacock, D. C. P. 1991. Displacements and segment linkage in strike-slip fault zones. *J. Struct. Geol.* **13**, 1025–1035.

Peacock, D. C. P. & Sanderson, D. J. 1991. Displacements, segment linkage and relay ramps in normal fault zones. *J. Struct. Geol.* **13**, 721–733.

Peacock, D. C. P. & Sanderson, D. J. 1994. Geometry and development of relay ramps in normal fault systems. *Bull. Am. Ass. Petrol. Geol.* **78**, 147–165.

Peppin, W. A., Honjas, W., Somerville, M. R. & Vetter, U. R. 1989. Precise master-event locations of aftershocks of the 4 October 1978 Wheeler Crest earthquake sequence near Long Valley, California. *Bull. seism. Soc. Am.* **79**, 67–76.

Petersen, K., Clausen, O.-R. & Korstgård, J. A. 1992. Evolution of a salt-related listric growth fault near the D-1 well, block 5605 Danish North Sea: displacement history and salt kinematics. *J. Struct. Geol.* **14**, 565–577.

Petit, J.-P., Massonnat, G., Pueo, F. & Rawnsley, K. 1994. Mode I fracture shape ratios in layered rocks: a case study in the Lodeve Permian Basin (France). Elf Internal Report. *BCREDP* **18**, 211–229.

Price, N. J. 1966. *Fault and Joint Development in Brittle and Semi-brittle Rock*. Pergamon Press, Oxford.

Purcaru, G. & Berckhemer, H. 1982. Quantitative relations of seismic source parameters and a classification of earthquakes. *Tectonophysics* **84**: 57–128.

Reasenberg, P. & Ellsworth, W. L. 1982. Aftershocks of the Coyote Lake, California, earthquake of August 6, 1979: a detailed study. *J. geophys. Res.* **87**, 10,637–10,655.

Rippon, J. H. 1985a. Contoured patterns of the throw and hade of normal faults in the Coal Measures (Westphalian) of north-east Derbyshire. *Proc. Yorks. geol. Soc.* **45**, 147–161.

Rippon, J. H. 1985b. New methods of forecasting the throw and hade of faults in some North Derbyshire Collieries. *Trans. Inst. Min. Engrs* **145**, 198–204.

Rogers, G. C., Cassidy, J. F. & Ellis, R. M. 1990. The Prince George, British Columbia, earthquake of 21 March 1986. *Bull. seism. Soc. Am.* **80**, 1144–1161.

Schwartz, D. P. & Coppersmith, K. J. 1984. Fault behavior and characteristic earthquakes: Examples from the Wasatch and San Andreas Fault Zones. *J. geophys. Res.* **89**, 5681–5698.

Segall, P. & Pollard, D. D. 1980. Mechanics of discontinuous faults. *J. geophys. Res.* **85**, 4337–4350.

Smith, K. D. & Priestley, K. F. 1993. Aftershock stress release along active fault planes of the 1984 Round Valley, California, earthquake sequence applying a time-domain stress drop method. *Bull. seism. Soc. Am.* **83**, 144–159.

Stein, R. S. & Ekstrom, G. 1992. Seismicity and geometry of a 110 km long blind thrust fault 2. Syntheseis of the 1982–1985 California earthquake sequence. *J. geophys. Res.* **97**, 4865–4883.

Takeo, M. & Mikami, N. 1987. Inversion of strong motion seismograms for the source process of the Naganoken–Seibu earthquake of 1984. *Tectonophysics* **144**, 271–285.

Trudgill, B. & Cartwright, J. 1994. Relay ramp forms and normal fault linkages; Canyonlands National Park, Utah. *Bull. geol. Soc. Am.* **106**, 1143–1157.

Tsai, Y. & Aki, K. 1970. Source mechanism of the Truckee, California, earthquake of September 12 1966. *Bull. seism. Soc. Am.* **60**, 1199–1208.

Vendeville, B. C. & Jackson, M. P. A. 1992. The rise of diapirs during thin-skinned extension. *Mar. Petrol. Geol.* **9**, 331–353.

Walsh, J. J. & Watterson, J. 1988. Analysis of the relationship between the displacements and dimensions of faults. *J. Struct. Geol.* **10**, 239–247.

Walsh, J. J. & Watterson, J. 1989. Displacement gradients on fault surfaces. *J. Struct. Geol.* **11**, 307–316.

Walsh, J. J. & Watterson, J. 1990. New methods of fault projection for coalmine planning. *Proc. Yorks. geol. Soc.* **48**, 209–219.

Warren, D. H., Scofield, C. & Bufe, C. G. 1985. Aftershocks of the 22 November 1977 earthquake at Willits, California: activity in the Maacama fault zone. *Bull. seism. Soc. Am.* **75**, 507–517.

Wells, D. L. & Coppersmith, K. J. 1994. New empirical relationships among magnitude, rupture length, rupture width, rupture area, and surface displacement. *Bull. seism. Soc. Am.* **84**, 974–1002.

Wesnousky, S. G. 1988. Seismological and structural evolution of strike-slip faults. *Nature* **335**, 340–343.

Westaway, R., Gawthorpe, R. & Tozzi, M. 1989. Seismological and field observations of the 1984 Lazio–Abruzzo earthquakes: implications for the active tectonics of Italy. *Geophys. J.* **98**, 489–514.

Wetmiller, R. J., Adams, J., Anglin, F. M., Hasegawa, H. S. & Stevens, A. E. 1984. Aftershock sequences of the 1982 Miramichi, New Brunswick, earthquakes. *Bull. seism. Soc. Am.* **74**, 621–653.

Wetmiller, R. J., Horner, R. B., Hasegawa, H. S., North R. G., Lamontagne, M., Weichert, D. H. & Evans, S. G. 1988. An analysis of the 1985 Nahanni earthquakes. *Bull. seism. Soc. Am.* **78**, 590–616.